



Heat transfer enhancement and pressure drop penalty in porous solar heaters: Numerical simulations

M. Bovand, S. Rashidi, J.A. Esfahani *

Department of Mechanical Engineering, Ferdowsi University of Mashhad, Mashhad 91775-1111, Iran

Received 12 June 2015; received in revised form 23 October 2015; accepted 29 October 2015

Communicated by: Associate Editor Yanjun Dai

Abstract

A comprehensive numerical study is performed on the fluid flow and heat transfer within a porous solar heater. The effects of porous material on the heat transfer enhancement and pressure drop are presented in details. Also, the attention is focused on the effects of several parameters on the combined convection–radiation heat transfer and flow structures. Volume averaged equations are applied to simulate the transport phenomena within the porous substrate. Furthermore, the regular continuity, momentum, and energy equations are used in the clear fluid region. These equations are discretized using the control volume technique. It is found that the Nusselt number increases by inserting the porous substrate to the heater. These augmentations are up to 3, 4.4 and 5.9 times for $\delta = 1/3$, $2/3$ and 1, respectively at $Da = 10^{-2}$. Also, the pressure drop increases with an increase in the porous layer thickness and decrease in the Darcy number.

© 2015 Elsevier Ltd. All rights reserved.

Keywords: Solar heater; Convection–radiation; Finite volume method; Pressure drop; Darcy number

1. Introduction

Heaters are a part of everyday modern life with a wide range of industrial and engineering applications. Examples include the oil and gas industries, chemical processing, hydrocarbon processing, polymers, pharmaceuticals, and food and beverage (Bhutta et al., 2012). The efficiency of heaters is an important topic in these devices and provides a new way to design and analyze them. The ideal heater transfers the maximum amount of heat with lowest pressure drop. A new type of these devices is solar heater with many advantages such as endless amounts of energy, no CO₂ emissions during operation, cost savings and many other benefits. Recently, porous materials have been used

in systems where the convection and radiation modes of heat transfer are both critical (Fuqiang et al., 2014; Lee et al., 2015; Hirasawa et al., 2013; Wang et al., 2013). These materials produce a pressure drop beside the heat transfer enhancement. A literature review on the related works to this topic is necessary in this stage.

Many studies have been conducted on the effects of porous material on the pressure drop or heat transfer (Xu et al., 2014; Chumpia and Hooman, 2015; Banerjee et al., 2015; Tsinoglou et al., 2004a,b; Martinopoulos et al., 2010; Missirlis et al., 2010; Missirlis et al., 2014). For example, forced convection in the developing region of a pipe partially filled with a porous layer has been investigated by Alkam and Al-Nimr (1998a). An external heating is used on the cylinder wall in their research. They found that the external heating has more effective penetration in the porous layer than that in the clear fluid region. In another

* Corresponding author.

E-mail address: abolfazl@um.ac.ir (J.A. Esfahani).

Nomenclature

C_F	Forchheimer coefficient (–)
c_p	specific heat at constant pressure (J/kg K)
D	height of the channel (m) $D = 2R_2$
Da	Darcy number (–) $Da = K/D^2$
f	friction factor (–)
h	heat transfer coefficient (W/m ² K)
k	thermal conductivity (W/m K)
K	permeability of the porous medium (m ²)
k_c	molecular thermal conductivity (W/m K)
k_r	radiative thermal conductivity (W/m K)
L	length of the heater (m)
Nu	Nusselt number (–) $Nu = \frac{q''(D)}{k_{eff}(T_w - T_m)}$
\overline{Nu}	surface-averaged Nusselt number (–)
$\langle \overline{Nu} \rangle$	time-averaged Nusselt number (–)
p	pressure (Pa)
Δp	pressure drop (Pa)
Pr	Prandtl number (–) $Pr = \nu/\alpha$
Rc	thermal conductivity ratio (–) $Rc = k_{eff}/k_f$
Re	Reynolds number (–) $Re = \rho U_\infty D/\mu$
R_1	thickness of the porous substrate (m)
R_2	half of the channel gap (m)
t	time (s)
t_p	period of time integration (s)
T	temperature (K)
u, v	velocity component in x and y directions, respectively (m/s)
x, y	rectangular coordinates components (m)

Greek symbols

α	thermal diffusivity of the fluid (m ² /s) $\alpha = k/\rho c_p$
β	stress jump parameter (–)
β_1	stress jump parameter related to inertia (–)
β_R	Rosseland mean extinction coefficient (1/m)
δ	dimensionless porous substrate thickness (–) $\delta = R_1/R_2$
ε	porosity (–)
μ	dynamic viscosity (kg/m s)
ν	kinematic viscosity (m ² /s)
σ	Stefan-Boltzmann coefficient (W/m ² K ⁴)
ρ	density of the fluid (kg/m ³)
λ	radiation parameter (–)
ζ	heat transfer enhancement (–)

Subscripts/superscripts

e	empty
eff	effective
f	fluid
m	mean
p	porous
s	solid
w	wall
∞	free stream
$*$	dimensional variables
1	clear fluid domain
2	porous domain

research, [Al-Nimr and Alkam \(1998b\)](#) investigated the fluid flow in the parallel-plate channels partially filled with the porous materials. They used Green's function method to obtain the analytical solution for modeling the fluid flow in the parallel-plate channels. Developing a 3-D computational model for the fluid flow and convective heat transfer in a channel partially filled with porous medium has been done by [Jen and Yan \(2005\)](#). It was found that there are two large vortices in the fluid region near the interface of the porous substrate with a pair of smaller vortices in porous substrate. This is due to the flow instability created by the blowing effect of the porous substrate. Convective heat transfer in a channel partially filled with a porous medium has been studied by [Aguilar-Madera et al. \(2011\)](#). They reported that the temperature profile is similar to the one found in a solid rod with the same dimensions as the channel for low values of the porosity. [Aghajani Delavar and Mohammadvali \(2013\)](#) simulated the convective heat transfer between two parallel plates with porous part using the Lattice Boltzmann Method. Their results showed that the temperature inside the porous block decreases with increase in Reynolds number. Recently, the local thermal non-equilibrium condition of porous media imbedded in the tube heaters has been studied by [Dehghan et al.](#)

(2014). They found that the influence of Darcy number on the velocity field is more than its influence on the temperature field. [Mahdavi et al. \(2014\)](#) presented the entropy generation and convective heat transfer inside a pipe partially filled with a porous material. The porous layer was placed at the core of the pipe or it was attached to the inner wall. They found that the placement of porous medium at the tube wall leads to higher values of Nusselt number for high values of conductivity ratio and Darcy number. [Torabi et al. \(2015\)](#) performed the heat transfer and entropy generation analyses for a channel partially filled with porous media under the local thermal non-equilibrium conditions. They observed that the values of local and total entropy generation rates increase with decrease in Darcy number.

Throughout the past couple of years, some researchers have investigated the convection heat transfer from a body embedded in a porous medium. For example, the forced convection heat transfer from a single circular obstacle embedded in a porous region has been studied by [Al-Sumaily et al. \(2012\)](#). Their results indicated that the porous particles suppress significantly the unsteady hydrodynamic and thermal behaviors inside the channel. [Rashidi et al. \(2013\)](#) performed a study on the fluid flow and forced

convection heat transfer around a solid cylinder wrapped with a porous substrate. They used porous substrate for thermal insulation or heat transfer augmentation. Their results revealed that the critical radius of insulation decreases with an increase in Darcy number. In another research, Valipour et al. (2014a) repeated this problem in the presence of a radial magnetic field. They reported that the effects of a magnetic field on the average Nusselt number are negligible for small Darcy numbers.

Some researchers studied the heat transfer in solar heaters or solar collectors. For example, solar collectors with tubes partially filled with porous layer have been appraised by Alkam and Al-Nimr (1999). They decreased the thermal resistance between the working fluid and the absorber panel with increase in the convective heat transfer coefficient within the tubes of the collector. In another study, Chen and Sutton (2005) enhanced the heat transfer in the entrance region of circular ducts by using porous ceramic. Their results showed that the insert of the porous material in optical thick working gas has relatively little effect on the enhancement of heat transfer. Convection–radiation heat transfer in a solar heater filled with a porous medium has been simulated by Dehghan et al. (2015). They found that the Nusselt number increases with the porous medium shape parameter. Note the porous media was used on all gaps between the two plates. Their study was focused on the thermal behavior. Recently, Rashidi et al. (2015a) performed a sensitivity analysis on the porous solar heaters. They observed that the sensitivity of the pressure drop ratio and Nusselt number to the Darcy number increases with an increase in the porous substrate thickness. Bahrehmand et al. (2015) performed both energy and exergy analyses for different solar air collector systems with forced convection. Li et al. (2015) examined the flow and heat transfer performances on the solar water heater with elliptical collector tube. Their study indicated that the value of Nusselt number increases with an increase in initial temperature. Kumar and Kim (2015) reviewed the various techniques to enhance the convective heat transfer in the solar air channels. They found that the baffle shapes with roughness have the best thermal performance. Acir and Ata (2015) remarkably improved the heat transfer rate in a new solar air heater by using circular type turbulators. Their results

revealed that the maximum heat transfer enhancement was in the vicinity of 416% for a specific turbulators arrangement. Valipour et al. (2014a) investigated Magneto-hydrodynamics flow and heat transfer around a solid circular cylinder wrapped with a porous substrate. They used the least square method (Brilakis et al., 2011; Rashidi et al., 2011, 2014c) to suggest empirical equations for average Nusselt number. The effect of magnetic field and Darcy numbers are taken into account for these equations.

The literature review showed that this subject of research has received attention due to the importance in different applications. However, a lack of information about this topic is visible and there is not a comprehensive study to cover all effective parameters. The results of this research can provide useful guidelines on how to design solar heaters, and be used as initial data for optimization analysis to determine the optimum conditions for maximum heat transfer rate and minimum pressure drop.

2. Problem statement

Consider a laminar, unsteady, and incompressible flow inside a parallel plate heater with impermeable surfaces, half thickness of 1 cm and a symmetric boundary. Also, the length of the channel (L) is 100 times larger than the half thickness (R_2). A porous substrate (sand stone) is placed at the plate with thickness R_1 . The fluid (water) enters the domain with a uniform velocity distribution (U_∞) and constant temperature (T_∞). A constant heat flux is used at the plate and it is uniform along the channel. Computational domain and coordinate system for the heater are shown in Fig. 1. The Cartesian coordinate system is placed at the symmetry axis and only the top half of the channel is considered for numerical calculations.

In this paper, the following assumptions are made:

- The porous layer is homogeneous, isotropic, and saturated with a single-phase fluid (Valipour et al., 2014b).
- The fully developed flow is desired.
- The fluid phase temperature is equal to that of the solid phase (local thermal equilibrium, LTE). Note that this condition is valid when the temperature difference between the fluid and solid phases is not notable

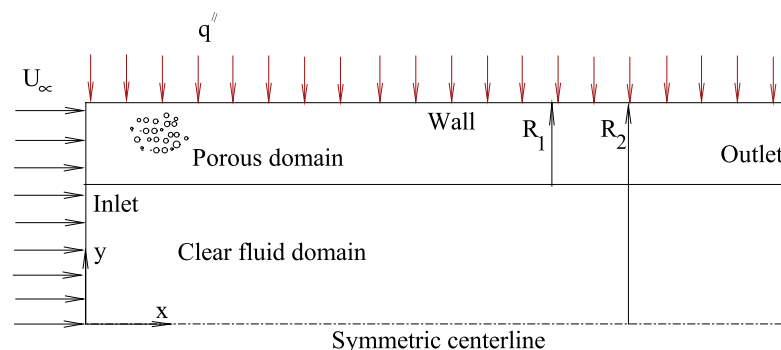


Fig. 1. Computational domain for the heater.

(Rashidi et al., 2014a). This assumption breaks down during the rapid cooling, heating or problems with significant temperature variation across the porous media. Therefore, this assumption is valid for the solar heater with a slow warming.

- A constant heat flux is imposed at the plate and it is uniform along the heater.
- The radiative heat transfer inside the porous layer is modeled by a diffusion process (See Appendix A).
- The analysis is performed for the Darcy number from $Da = 10^{-6}$ to $Da = 10^{-2}$ and radiation parameter from $\lambda = 0.5$ to $\lambda = 0.9$. In addition, the thermal conductivity ratio and Prandtl number were set equal to 5 and 7, respectively. Also, two values of 40 and 100 are considered for Reynolds number. Note that the ratio of thermal conductivity is fixed at 5 which means the solid phase (sand stone) is a better heat conductor than the fluid (water).
- The reflectors concentrate the solar energy to both sides of the heater. The heat loss is minimized by using the glass cover and suitable gap distance or evacuation. Thus, the net solar heat flux has been used on the heater and the attentions are focused on the internal side.

3. Mathematical model

Governing equations including the continuity, momentum, and energy are derived to simulate this problem. A two-domain approach is applied to pertinent the governing equations in this study. Therefore, the governing equations must be solved for two zones: the clear fluid and porous medium zones. Hence, two sets of equations are considered. A set for clear fluid zone which are indicated by subscript (1) and another set for porous medium which are denoted by subscript (2). With the above description, the following equations can be written as below.

3.1. Governing equations

3.1.1. Governing equations for the clear region

Mass conservation equation is:

$$\frac{\partial u_1^*}{\partial x^*} + \frac{\partial v_1^*}{\partial y^*} = 0 \quad (1)$$

The momentum equations in the x and y directions are:

$$\rho_f \left(\frac{\partial u_1^*}{\partial t^*} + u_1^* \frac{\partial u_1^*}{\partial x^*} + v_1^* \frac{\partial u_1^*}{\partial y^*} \right) = - \frac{\partial p_1^*}{\partial x^*} + \mu \left(\frac{\partial^2 u_1^*}{\partial x^{*2}} + \frac{\partial^2 u_1^*}{\partial y^{*2}} \right) \quad (2)$$

$$\rho_f \left(\frac{\partial v_1^*}{\partial t^*} + u_1^* \frac{\partial v_1^*}{\partial x^*} + v_1^* \frac{\partial v_1^*}{\partial y^*} \right) = - \frac{\partial p_1^*}{\partial y^*} + \mu \left(\frac{\partial^2 v_1^*}{\partial x^{*2}} + \frac{\partial^2 v_1^*}{\partial y^{*2}} \right) \quad (3)$$

The energy equation:

$$\rho_f c_p \left(\frac{\partial T_1^*}{\partial t^*} + u_1^* \frac{\partial T_1^*}{\partial x^*} + v_1^* \frac{\partial T_1^*}{\partial y^*} \right) = k_f \left(\frac{\partial^2 T_1^*}{\partial x^{*2}} + \frac{\partial^2 T_1^*}{\partial y^{*2}} \right) \quad (4)$$

where superscript “*” denotes the dimensional variables. Also, μ , c_p , k_f and ρ_f are viscosity, specific heat, thermal conductivity and density of the fluid phase, respectively.

3.1.2. Governing equations for the porous substrate

Mass conservation equation in the porous substrate is:

$$\frac{\partial u_2^*}{\partial x^*} + \frac{\partial v_2^*}{\partial y^*} = 0 \quad (5)$$

The momentum equations in the x and y directions in the porous substrate are:

$$\begin{aligned} \frac{\rho_f}{\varepsilon^2} \left(\varepsilon \frac{\partial u_2^*}{\partial t^*} + u_2^* \frac{\partial u_2^*}{\partial x^*} + v_2^* \frac{\partial u_2^*}{\partial y^*} \right) &= - \frac{\partial p_2^*}{\partial x^*} + \frac{\mu}{\varepsilon} \left(\frac{\partial^2 u_2^*}{\partial x^{*2}} + \frac{\partial^2 u_2^*}{\partial y^{*2}} \right) \\ &\quad - \frac{\mu}{K} u_2^* - \frac{C_F \rho_f}{\sqrt{K}} \sqrt{u_2^{*2} + v_2^{*2}} u_2^* \end{aligned} \quad (6)$$

Darcy term Forchheimer term Brinkman term

$$\begin{aligned} \frac{\rho_f}{\varepsilon^2} \left(\varepsilon \frac{\partial v_2^*}{\partial t^*} + u_2^* \frac{\partial v_2^*}{\partial x^*} + v_2^* \frac{\partial v_2^*}{\partial y^*} \right) &= - \frac{\partial p_2^*}{\partial y^*} + \frac{\mu}{\varepsilon} \left(\frac{\partial^2 v_2^*}{\partial x^{*2}} + \frac{\partial^2 v_2^*}{\partial y^{*2}} \right) \\ &\quad - \frac{\mu}{K} v_2^* - \frac{C_F \rho_f}{\sqrt{K}} \sqrt{u_2^{*2} + v_2^{*2}} v_2^* \end{aligned} \quad (7)$$

Darcy term Forchheimer term Brinkman term

where ε and K are porosity and permeability, respectively.

The volume-averaged fluid velocity (\bar{v}) inside the porous layer is related to the Darcy velocity (\vec{v}) through Dupuit-Forchheimer relationship, as $\vec{v} = \varepsilon \bar{v}$. Forchheimer coefficient, C_F , is calculated by (Rashidi et al., 2014b):

$$C_F = \frac{1.75}{\sqrt{150\varepsilon^3}} \quad (8)$$

The energy equation, subject to the local thermal equilibrium condition, may be written as:

$$\frac{\rho_f c_p}{\varepsilon} \left(\varepsilon \frac{\partial T_2^*}{\partial t^*} + u_2^* \frac{\partial T_2^*}{\partial x^*} + v_2^* \frac{\partial T_2^*}{\partial y^*} \right) = k \left(\frac{\partial^2 T_2^*}{\partial x^{*2}} + \frac{\partial^2 T_2^*}{\partial y^{*2}} \right) \quad (9)$$

The above governing equations are made dimensionless by using the following dimensionless variables:

$$\begin{aligned} x &= \frac{x^*}{D_h}, \quad y = \frac{y^*}{D_h}, \quad u = \frac{u^*}{U_\infty}, \quad v = \frac{v^*}{U_\infty}, \quad p = \frac{p^*}{\rho U_\infty^2}, \\ t &= \frac{t^* U_\infty}{D_h}, \quad T = \frac{T^* - T_w^*}{T_m^* - T_w^*} \end{aligned} \quad (10)$$

Then, the governing equations reduce to the following dimensionless equations.

3.1.3. Dimensionless equations for the clear domain

Mass conservation equation:

$$\frac{\partial u_1}{\partial x} + \frac{\partial v_1}{\partial y} = 0 \quad (11)$$

The momentum equations in the x and y directions:

$$\left(\frac{\partial u_1}{\partial t} + u_1 \frac{\partial u_1}{\partial x} + v_1 \frac{\partial u_1}{\partial y}\right) = -\frac{\partial p_1}{\partial x} + \frac{1}{Re} \left(\frac{\partial^2 u_1}{\partial x^2} + \frac{\partial^2 u_1}{\partial y^2}\right) \quad (12)$$

$$\left(\frac{\partial v_1}{\partial t} + u_1 \frac{\partial v_1}{\partial x} + v_1 \frac{\partial v_1}{\partial y}\right) = -\frac{\partial p_1}{\partial y} + \frac{1}{Re} \left(\frac{\partial^2 v_1}{\partial x^2} + \frac{\partial^2 v_1}{\partial y^2}\right) \quad (13)$$

The energy equation:

$$\left(\frac{\partial T_1}{\partial t} + u_1 \frac{\partial T_1}{\partial x} + v_1 \frac{\partial T_1}{\partial y}\right) = \frac{1}{RePr} \left(\frac{\partial^2 T_1}{\partial x^2} + \frac{\partial^2 T_1}{\partial y^2}\right) \quad (14)$$

3.1.4. Governing equations for the porous layer

Mass conservation equation:

$$\frac{\partial u_2}{\partial x} + \frac{\partial v_2}{\partial y} = 0 \quad (15)$$

The momentum equations in the x and y directions:

$$\frac{1}{\varepsilon} \left(\varepsilon \frac{\partial u_2}{\partial t} + u_2 \frac{\partial u_2}{\partial x} + v_2 \frac{\partial u_2}{\partial y}\right) = -\frac{\partial p_2}{\partial x} + \frac{1}{\varepsilon Re} \left(\frac{\partial^2 u_2}{\partial x^2} + \frac{\partial^2 u_2}{\partial y^2}\right) - \frac{1}{ReDa} u_2 - \frac{C_F}{\sqrt{Da}} \sqrt{u_2^2 + v_2^2} u_2 \quad (16)$$

$$\frac{1}{\varepsilon} \left(\varepsilon \frac{\partial v_2}{\partial t} + u_2 \frac{\partial v_2}{\partial x} + v_2 \frac{\partial v_2}{\partial y}\right) = -\frac{\partial p_2}{\partial y} + \frac{1}{\varepsilon Re} \left(\frac{\partial^2 v_2}{\partial x^2} + \frac{\partial^2 v_2}{\partial y^2}\right) - \frac{1}{ReDa} v_2 - \frac{C_F}{\sqrt{Da}} \sqrt{u_2^2 + v_2^2} v_2 \quad (17)$$

The energy equation can be written as:

$$\frac{1}{\varepsilon} \left(\varepsilon \frac{\partial T_2}{\partial t} + u_2 \frac{\partial T_2}{\partial x} + v_2 \frac{\partial T_2}{\partial y}\right) = \frac{Rc}{RePr} \left(\frac{\partial^2 T_2}{\partial x^2} + \frac{\partial^2 T_2}{\partial y^2}\right) \quad (18)$$

where Da , Re , and Pr are Darcy, Reynolds, and Prandtl numbers, respectively, defined by:

$$Da = \frac{K}{D^2}, \quad Re = \frac{\rho U_\infty D}{\mu}, \quad Pr = \frac{\nu}{\alpha} \quad (19)$$

where ν and α are kinematic viscosity and thermal diffusivity of the fluid, respectively.

Also, Nusselt number based on the hydraulic diameter of the heater is defined by:

$$Nu = \frac{q''(D)}{k_{eff}(T_w - T_m)} \quad (20)$$

where T_m is mean temperature, defined by (Dehghan et al., 2015):

$$T_m = \frac{1}{R_2 u_m} \int_0^{R_2} u T dy \quad (21)$$

u_m is the mean velocity, given by:

$$u_m = \frac{1}{R_2} \int_0^{R_2} u dy \quad (22)$$

Also, the surface-averaged Nusselt number (\overline{Nu}) is defined as follows (Bovand et al., 2015a):

$$\overline{Nu} = \frac{1}{A} \int_A Nu dA \quad (23)$$

Therefore, the time-averaged Nusselt number ($\langle \overline{Nu} \rangle$) is calculated by (Bovand et al., 2015a):

$$\langle \overline{Nu} \rangle = \frac{1}{t_p} \int_0^{t_p} \overline{Nu} dt \quad (24)$$

where A and t_p are the heater surface and the period of time integration.

3.2. Boundary conditions

The boundary conditions for this problem could be written as follows:

At the inlet of the heater, the uniform flow is used:

$$\begin{aligned} \text{For } 0 < y < (R_2 - R_1) &\Rightarrow u_1 = 1, \quad v_1 = 0, \quad T_1 = 0 \\ \text{For } (R_2 - R_1) < y < R_2 &\Rightarrow u_2 = 1, \quad v_2 = 0, \quad T_2 = 0 \end{aligned} \quad (25)$$

At the outlet of the heater, zero gradient boundary conditions are used. These boundary conditions are given by (Rashidi et al., 2015b):

$$\begin{aligned} \text{For } 0 < y < (R_2 - R_1) &\Rightarrow \frac{\partial u_1}{\partial x} = 0, \quad \frac{\partial v_1}{\partial x} = 0, \quad \frac{\partial T_1}{\partial x} = 0 \\ \text{For } (R_2 - R_1) < y < R_2 &\Rightarrow \frac{\partial u_2}{\partial x} = 0, \quad \frac{\partial v_2}{\partial x} = 0, \quad \frac{\partial T_2}{\partial x} = 0 \end{aligned} \quad (26)$$

At the centerline of the heater, symmetry conditions have been used. These conditions are given by:

$$\frac{\partial u_1}{\partial y} = 0, \quad \frac{\partial T_1}{\partial y} = 0 \quad (27)$$

For the heater wall, no-slip and constant heat flux are used as the velocity and thermal boundary conditions. These conditions are defined by:

$$u_2 = 0, \quad v_2 = 0, \quad -(k_c + k_r) \frac{\partial T_2}{\partial y} = q''_w \quad (28)$$

Also, k_c and k_r are the effective solid and radiative conductivities, respectively. k_r is calculated by (Nield and Kuznetsov, 2010):

$$k_r = \frac{16\sigma T^{*3}}{3\beta_R} \quad (29)$$

where β_R and σ are the Rosseland mean extinction coefficient and the Stefan Boltzmann constant, respectively.

Radiation parameter can be written as follows:

$$\lambda = \frac{1}{1 + 3\beta_R k_c / 16\sigma T_w^3} \quad (30)$$

Different boundary conditions between a fluid layer and a porous medium are investigated by Alazmi and Vafai (2001). It was found that for most practical applications, the variances within different thermal interfacial-conditions have negligible effects on the results. Rashidi et al. (2015b) performed a comparison for the fluid flow interface boundary conditions between the porous and clear fluid regions. Their results indicated that the stress-jump model is superior to other models. Therefore, the stress-jump boundary condition was applied in this study. Also, the coupling conditions at the interface region follow the continuity of the velocity, the shear stress, the temperature and the heat flux. These conditions are given by:

$$\begin{aligned} u_1 &= u_2, \quad v_1 = v_2 \\ \left\{ \begin{array}{l} \mu_{\text{eff}} \frac{\partial v_2}{\partial y} - \mu_f \frac{\partial v_1}{\partial y} = \beta \frac{\mu_f}{\sqrt{K}} v_1 + \beta_1 \rho v_1^2 \\ \text{or} \\ \mu_{\text{eff}} \frac{\partial v_2}{\partial y} - \mu_f \frac{\partial v_1}{\partial y} = \beta \frac{\mu_f}{\sqrt{K}} v_2 + \beta_1 \rho v_2^2 \end{array} \right. \quad (31) \\ T_1 &= T_2, \quad \frac{\partial T_1}{\partial x} = Rc \frac{\partial T_2}{\partial x}, \quad \frac{\partial T_1}{\partial y} = Rc \frac{\partial T_2}{\partial y} \end{aligned}$$

where β and β_1 are adjustable parameters which account for the stress jump at the interface. Both β and β_1 are equal to 1 in the present study (Rashidi et al., 2015b). Also, the effective dynamic viscosity is used in the following form (Rashidi et al., 2015c):

$$\mu_{\text{eff}} = \frac{\mu_f}{\varepsilon} \quad (32)$$

As the initial condition, there is no flow inside the domain at the initial time.

4. Computational model

4.1. Numerical method

The governing equations with the relevant boundary conditions are discretized using the finite volume method. A two-dimensional staggered grid has been employed in this paper. In this method, the scalar variables are stored in the centers of the control volumes, whereas the velocity, momentum and temperature variables are located at the control volume faces. Also, the well-known SIMPLE algorithm is applied to couple the velocity and pressure (Patankar, 1980). The first order implicit method is adopted to discretize the time derivatives and a third-order accurate QUICK scheme is used for the convective estimation (Rashidi et al., 2015d; Rashidi and Esfahani, 2015; Rashidi et al., 2015e; Bovand et al., 2015b). Green-Gauss is employed to discretize the diffusion terms. Note that the converged solutions are acceptable when the summation of residuals to be lower than 10^{-7} for all equations.

4.2. Grid independent study and validation

A close-up view of the grid resolution at the inlet of the heater as a sample mesh is shown in Fig. 2. A two-dimensional square mesh has been generated for this study. This mesh is refined near the heater walls and interface between the porous substrate and fluid region. Several grid sizes were tested to insure that the results are independent of the grid size. This test is performed for the cases empty heater ($\delta = 0$) and the heater with porous substrate ($\delta = 1/3$ and $Da = 10^{-3}$) at $Re = 100$. As shown in Table 1, the percentage differences between cases 3 and 4 for the Nusselt number are 0.2% and 0.3% for $\delta = 0$ and $1/3$, respectively. Therefore, the grid size of 1200×160 is selected for the rest of simulations.

In order to display the validity of the numerical method, present results are compared with some of the experimental results. Validation is performed for an open-cell aluminum foam cylinder heated at the wall by a constant heat flux and cooled by the water flow. A tube with a length of 30.50 cm, diameter of 5.08 cm and wall thickness of 0.63 cm is considered. Foam is inserted to the tube's internal surface. This foam is made by aluminum alloy 6101-T6 with porosity of 87.6%.

The results are obtained for inlet velocity of 0.0049 m/s and the local thermal equilibrium employed by the numerical solution. More details about the geometry of this problem are available in Dukhan et al. (2015). The results are available in Fig. 3. The percentage errors between the numerical and experimental results at different axial distances are presented in Table 2. As shown in this table, the present numerical results follow the trends of experiment along the length of the channel with the average error in the vicinity of 8%. This indicates that the numerical results agree well with the experimental data. Note that there is always a discrepancy between numerical and experimental results. This discrepancy is due to the experimental factors like calibrating equipment for lab measurements, experiment accuracy, human errors, missing out some process, etc. Of course, numerical errors can lead to this dis-

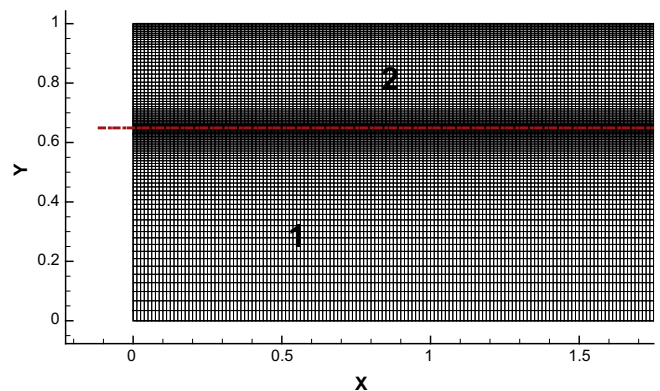


Fig. 2. Mesh sample at the inlet of the heater.

Table 1
Effect of grid size on Nusselt number at $Re = 100$.

No.	Grid size	Nusselt number			
		$\delta = 0$	Percentage difference	$\delta = 1/3, Da = 10^{-3}$	Percentage difference
1	150×20	0.722	1.3	1.153	1.4
2	300×40	0.732	0.8	1.17	0.9
3	600×80	0.737	0.2	1.179	0.3
4	1200×160	0.739		1.183	

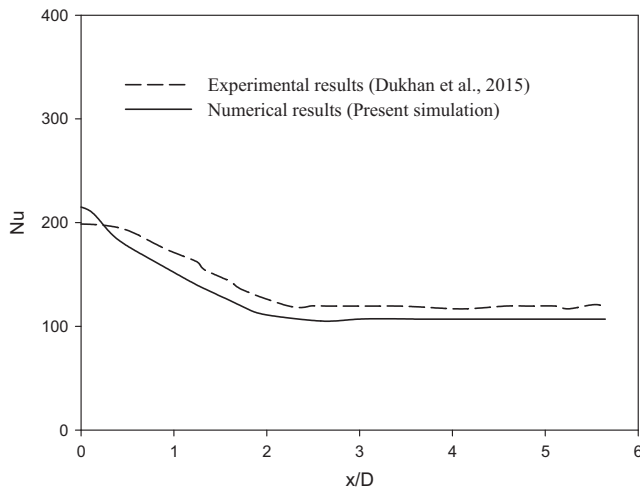


Fig. 3. Comparison between the present results and experimental data by Dukhan et al. (2015).

Table 2
Percentage errors between the numerical and experimental results of Fig. 3.

x/D	Percentage errors
0	8.2
1	8.91
2	7.92
3	8.42
4	7.45
5	8.66

crepancy. However, 8% error between numerical and experimental results is acceptable.

5. Results and discussion

A numerical simulation has been performed to investigate the effects of porous substrate on the heat transfer and flow characteristics.

Fig. 4 presents the streamlines inside the heater for different dimensionless porous substrate thicknesses and three Darcy numbers at $Re = 40$. Note that these values of Darcy numbers are selected as low, intermediate and high values. As shown in this figure, the streamlines within the porous substrate are more elongated in the horizontal direction for high Darcy numbers (i.e. $Da = 10^{-2}$). The streamlines more easily penetrate into the porous substrate for higher Darcy numbers. It is worth mentioning that the curvature

of the streamlines increases with a decrease in Darcy numbers because more obstruction to the fluid flow is expected for low Darcy number. Note that this obstruction is due to the viscous and inertial forces created by the porous solid matrix. Also, the streamlines are more uniform for the case of full packed channel ($\delta = 1$). The streamlines are much denser at the clear fluid region for $\delta = 2/3$ and $Da = 10^{-6}$. The porous substrate acts as a solid block and the path of the flow in clear fluid region (cross-sectional area in the fluid region) decreases for low Darcy number (i.e. $Da = 10^{-6}$). The streamlines for the case of $Da = 10^{-2}$ and $\delta = 1$ are similar to the case of empty heater $\delta = 0$ because a porous layer with high Darcy number (high permeability) acts as a void body. For all cases, the streamlines have a uniform behavior inside the heater at the horizontal direction.

The velocity contours inside the heater for different porous substrate thicknesses and Darcy numbers at $Re = 40$ are shown in Fig. 5. As shown in this figure, the velocity inside the porous substrate is small compared to the clear fluid region for $\delta = 1/3$ and $2/3$. This is due to the strong resistance of the porous substrate. Also, the velocity increases in the fluid region with an increase in dimensionless porous substrate thickness for $\delta = 1/3$ and $2/3$. This is due to the smaller cross-sectional area in the fluid region for larger dimensionless porous substrate thicknesses. This leads to a larger velocity value in the clear fluid region. Also, this figure shows the boundary layer thickness. It is observed that the boundary layer thickness increases with decrease in Darcy numbers. For $Da = 10^{-6}$, the porous substrate acts like a solid body near the walls and the fluid velocity is near the zero in this region. Also, it is noticeable that the boundary layer thickness increases by using porous substrate compared with that in the corresponding empty heater.

Axial velocity distributions in the vertical direction for different Darcy numbers and porous substrate thicknesses at $Re = 100$ and $x/R_2 = 5$ are shown in Fig. 6. It is observed that the mean fluid velocity in the porous substrate is lower than that in the clear fluid region. It is noticeable that the flow retards by the microscopic viscous and inertial forces generated by the porous solid matrix. It can be seen that for a constant porous substrate thickness, the divergence between the velocity profiles around the interface region increases with decrease in Darcy number. This is due to the jump in shear stress at the interface region (see Eq. (31)). Note that terms of $\mu_{\text{eff}}\partial v_2/\partial y$ and $\mu_f\partial v_1/\partial y$ in Eq. (31) denote the shear stresses of the porous

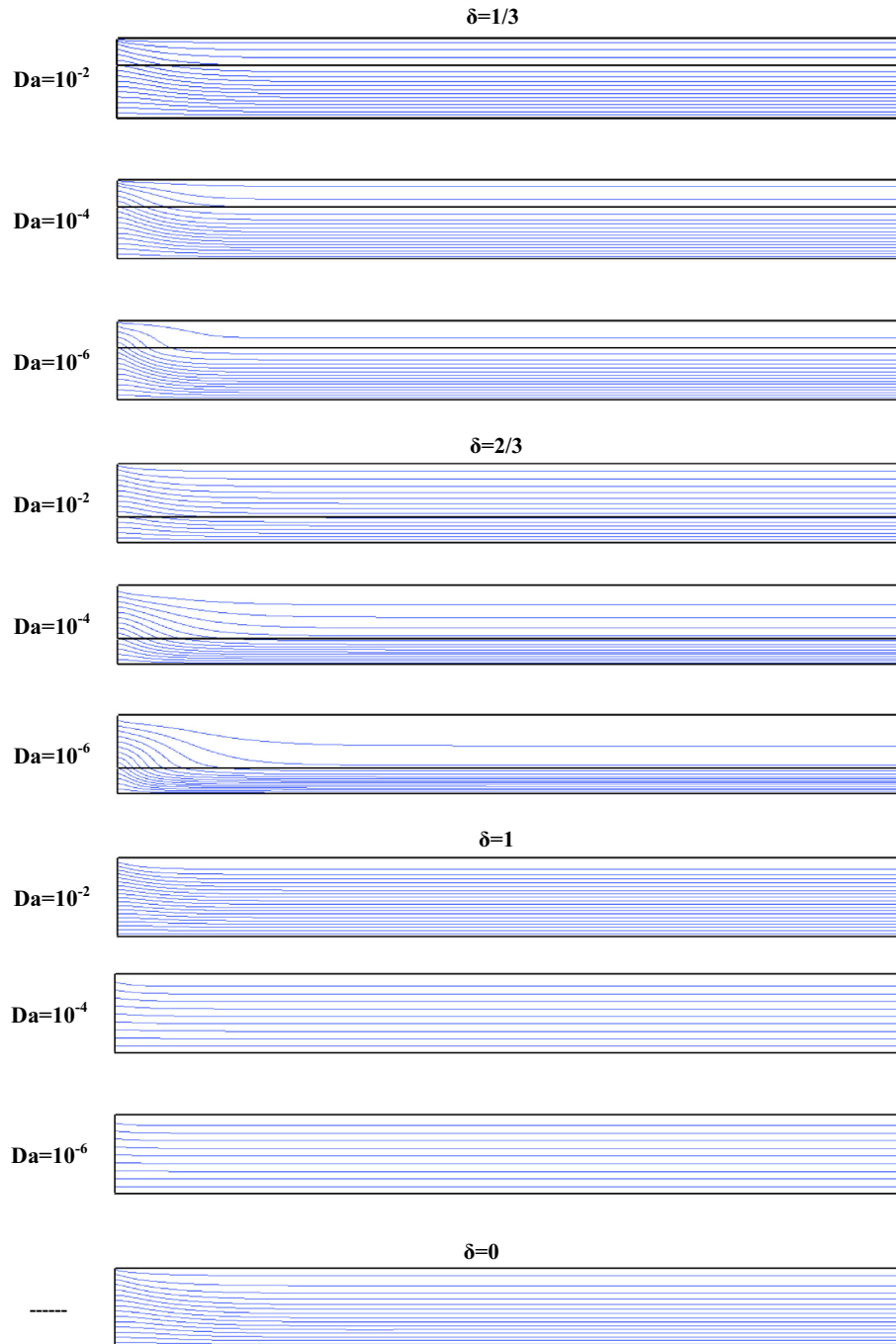


Fig. 4. Streamlines inside the heater for different Darcy numbers and porous substrate thicknesses at $Re = 40$.

and clear fluid regions, respectively. Also, $\beta^{\mu_f} / \sqrt{K}^{v_1}$ and $\beta_1 \rho v_1^2$ are defined as viscous and inertial terms, respectively. The right-hand side of Eq. 31 increases with decrease in Darcy number (permeability) and this leads to the difference between two shear stresses (the shear stresses for the porous and clear fluid regions). It is worth mentioning that the velocity decreases with increase in Darcy number at the clear fluid region for $\delta = 1/3$ and $2/3$. For the porous region, the velocity increases with an increase in Darcy number for this case ($\delta = 1/3$ and $2/3$). Moreover, the velocity for the full fill heater ($\delta = 1$) is lower than that

for the empty heater ($\delta = 0$) in the core region of the channel. This makes the near wall velocity to be higher for full fill heater, which can contribute to advection of heat. Lower Darcy number at full fill heater can flatten the velocity profile in the core region, which is similar to behavior of the turbulent channel flow.

The isotherm contours inside the heater for different porous substrate thicknesses and Darcy numbers at $Re = 40$ and $\lambda = 0.5$ are presented in Fig. 7. It can be seen that the size of the thermally developing entrance increases with an increase in Darcy number. It is obvious that the fluid passing

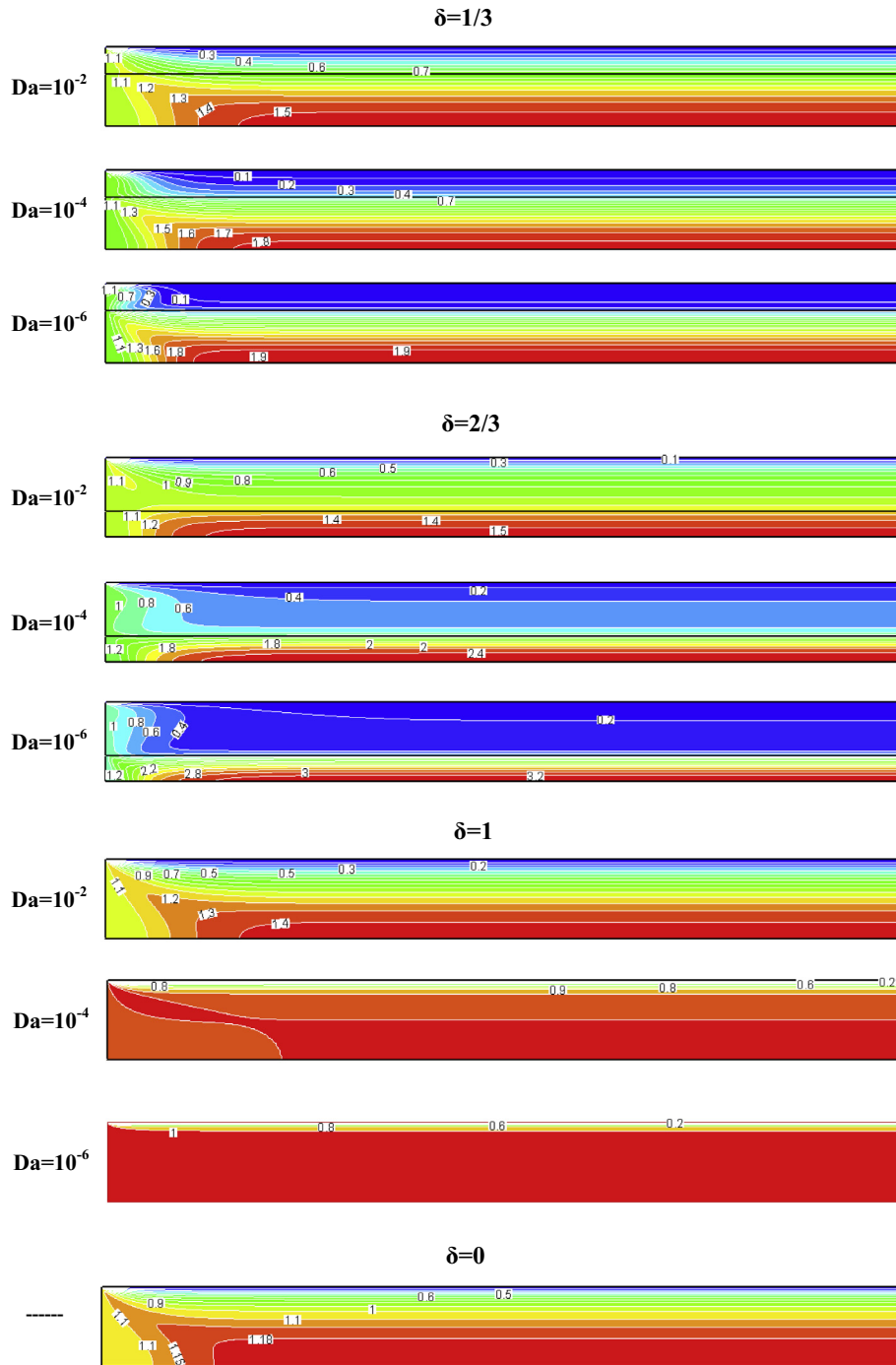


Fig. 5. Velocity contours inside the heater for different Darcy numbers and porous substrate thicknesses at $Re = 40$.

through the heater is negligible for low value of Darcy number (i.e. $Da = 10^{-6}$). As more and more fluid penetrate inside the heater for higher Darcy number, they carry away more heat with themselves. Therefore, a long thermally developing entrance is observed at high Darcy number. For all cases, the isotherms show a steady thermally developing entrance inside the heater at the horizontal direction. It is evident that the isotherm contours are normal to the symmetric centerline because this line acts as an insulated wall

(see Eq. (27)). It is worth mentioning that the temperature distribution in porous substrate becomes more uniform with an increase in Darcy numbers. Also, the isotherm lines are more stretched in flow direction for higher values of Darcy number because it is easier for fluid to flow in the heater with larger velocity at high Darcy numbers. The contours are much more sporadic when the heater is full filled by porous material ($\delta = 1$). Note that the heat conduction plays an important role when the porous materials are inserted to

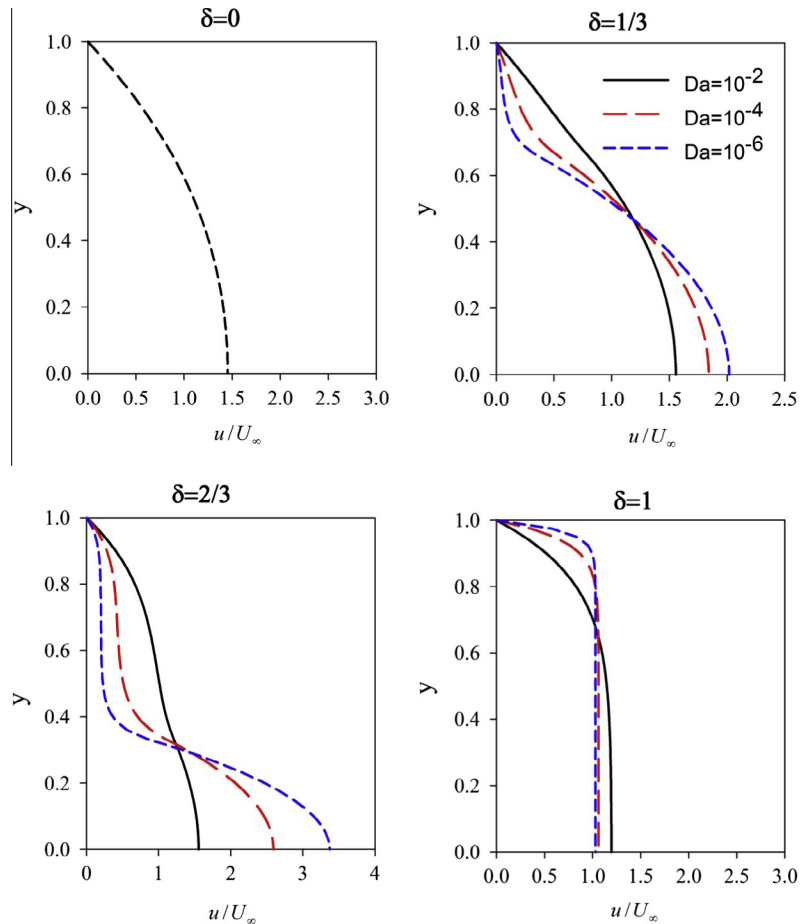


Fig. 6. Axial velocity distribution in the vertical direction for different Darcy numbers and porous layer thicknesses at $Re = 100$ and $x/R_2 = 5$.

the heater especially at low values of Darcy number. Moreover, the insert of porous material has forced the temperature gradient near the wall to increase.

Variations of time-averaged Nusselt number against Darcy number for different porous substrate thicknesses at $Re = 100$ and $\lambda = 0.5$ are presented in Fig. 8. Note that the horizontal line denotes empty heater ($\delta = 0$). As shown in this figure, the Nusselt number increases by adding the porous substrate to the heater for high Darcy numbers. This is justified by two reasons. First, the heat transfer from the porous substrate to the fluid flow increases due to the larger effective conductivity of this medium. Second, the heat transfer rate is increased with increase in Darcy numbers because the fluid flows faster through porous substrate with high permeability. Therefore, the rate of convection heat transfer is considerably increased with an increase in Darcy number. It is worth mentioning that the Nusselt number increases with an increase in porous substrate thicknesses for higher values of Darcy number. These augmentations are up to 3, 4.4 and 5.9 times for $\delta = 1/3$, $2/3$ and 1, respectively at $Da = 10^{-2}$. However, increase in the porous substrate thicknesses leads to a small reduction in Nusselt number for Darcy numbers smaller than 10^{-5} .

Variations of the local Nusselt number in the heater wall for different porous layer thicknesses at $Re = 100$, $\lambda = 0.5$ and $Da = 10^{-3}$ are shown in Fig. 9. As shown in this figure, Nusselt number increases with an increase in the porous substrate thicknesses for this Darcy number. Note that the heat convection plays an important role at high Darcy numbers and that for $\delta = 0$, the Nusselt number decreases along the axial direction for $x/R_2 < 4$ while it is generally constant for $x/R_2 > 4$ along the axial direction (thermally developed Nusselt number value). Also, this specific value of x/R_2 increases with an increase in porous substrate thicknesses. In addition, there are Nusselt numbers for laminar flow between parallel plates or inside the tube for the case of constant heat flux wall in the references (Bejan, 2013). These Nusselt numbers are for the cases of empty channel ($\delta = 0$) and without considering radiation ($\lambda = 0$). For example, thermally developed Nusselt number value for laminar flow inside a tube with constant heat flux wall is equal to 4.364 (Bejan, 2013).

Variations of the local Nusselt number at the heater wall for different porous layer thicknesses and at $Re = 100$, $\lambda = 0.5$ and $Da = 10^{-6}$ are shown in Fig. 10. As shown in this figure, Nusselt number decreases with an increase in the porous substrate thicknesses for this Darcy number.

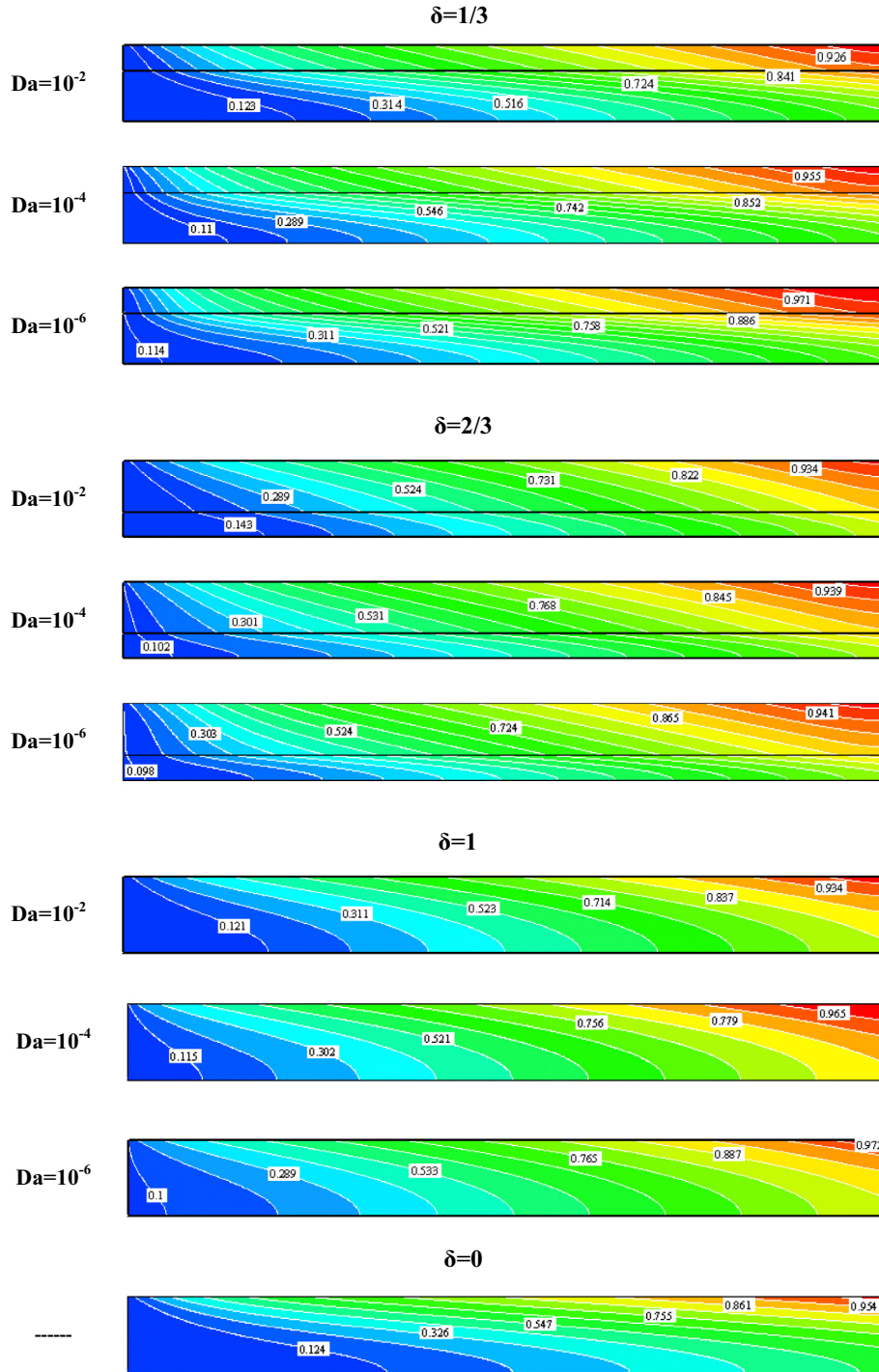


Fig. 7. Temperature contours inside the heater for different Darcy numbers and porous substrate thicknesses at $Re = 40$ and $\lambda = 0.5$.

Note that the heat transfer rate from the wall to fluid is constant but the temperature difference of flow increases because the fluid has more time to get heat from the wall at low Darcy number. Also, the heat conduction plays an important role at low Darcy numbers.

The effects of the radiation parameter (λ) on the time-averaged Nusselt number for different Darcy numbers at $Re = 100$ are shown at Fig. 11. It can be seen that the averaged Nusselt number increases with an increase in radiation parameter. These augmentations are in the vicinity

of 78.8%, 61.8% and 44.4% for Darcy numbers equal to 10^{-4} , 10^{-3} and 10^{-2} , respectively at $0.5 < \lambda < 0.9$. Therefore, the effects of the radiation parameter on augmentation of heat transfer are more visible for lower Darcy number.

Variations of pressure drop versus dimensionless porous layer thickness for different Darcy numbers at $Re = 100$ are presented in Fig. 12. Here, the pressure drop ratio is the ratio of the pressure drop in porous heater to that in the empty heater ($\delta = 0$). It is observed that the pressure drop

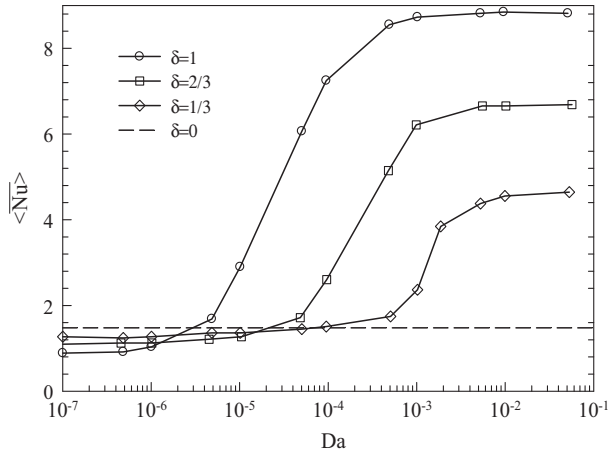


Fig. 8. Variations of time-averaged Nusselt number against Darcy numbers for different porous layer thicknesses at $Re = 100$, $Rc = 5$ and $\lambda = 0.5$.

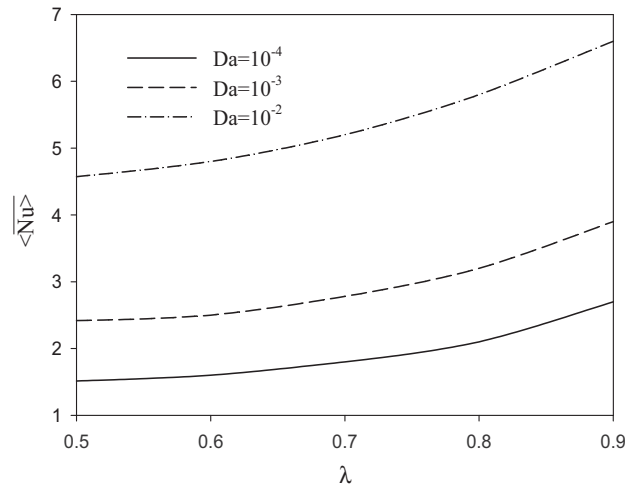


Fig. 11. Variations of time-averaged Nusselt number against radiation parameter for different Darcy numbers at $Re = 100$, $Rc = 5$ and $\delta = 1/3$.

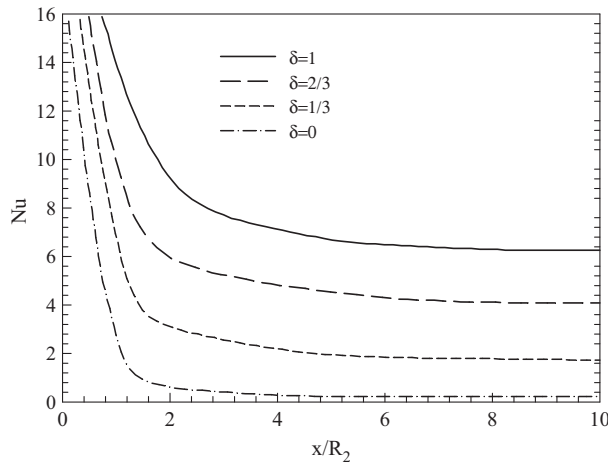


Fig. 9. Variations of local Nusselt number at heater wall for different porous layer thicknesses at $Re = 100$, $Rc = 5$, $\lambda = 0.5$ and $Da = 10^{-3}$.

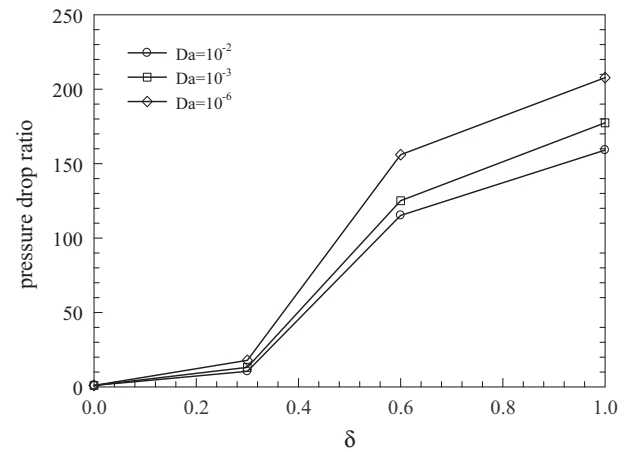


Fig. 12. Variations of pressure drop versus porous layer thickness for different Darcy numbers at $Re = 100$.

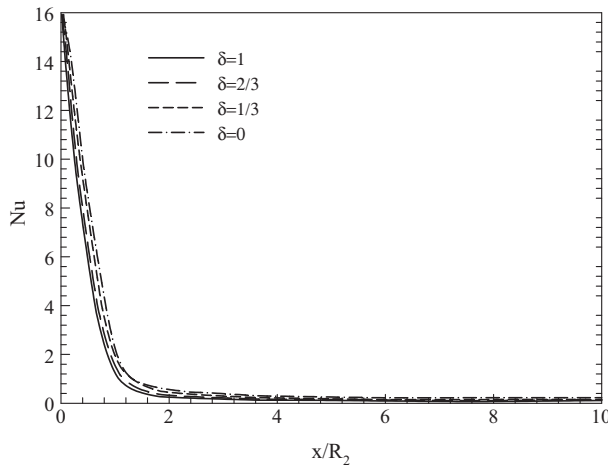


Fig. 10. Variations of local Nusselt number at heater wall for different porous layer thicknesses at $Re = 100$, $Rc = 5$, $\lambda = 0.5$ and $Da = 10^{-6}$.

for the porous heater increases with a decrease in Darcy numbers. This is due to the high macroscopic and microscopic shears, and high bulk and microscopic inertial drag forces for the low Darcy numbers. Also, the pressure drop increases with an increase in porous layer thickness. Therefore, more pumping work is required for the porous heater to maintain the same amount of the flow rate in empty heater. As a result, an important factor that must be considered when use of the porous material to increase in heat transfer is the penalty arising from the enhanced pressure drop. Therefore, the porous materials have a positive impact upon the heat transfer enhancement and a negative effect on pressure drop, consequently on the pumping power. Note that the high value of pressure drop occurs at high value of porous layer thicknesses (i.e. $\delta = 1$ or $2/3$). Use of a small porous layer thickness (i.e. $\delta = 1/3$) with moderate increase in heat transfer rate is recommended for cases that term of pressure drop is critical.

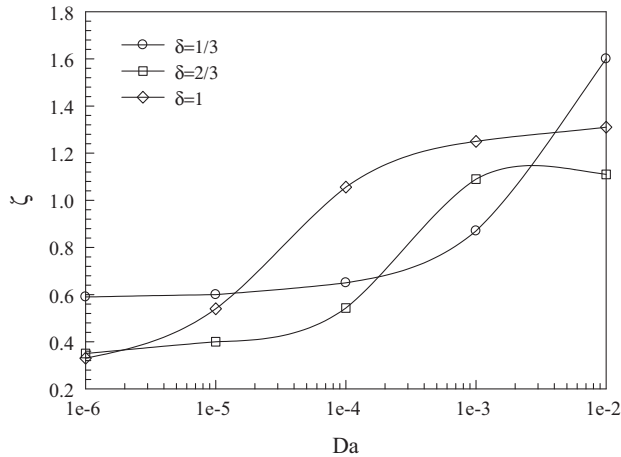


Fig. 13. Variations of heat transfer enhancement versus Darcy numbers for different porous layer thicknesses at $Re = 100$.

Variations of the heat transfer enhancement (ζ) versus Darcy numbers for different porous layer thickness at $Re = 100$ are presented in Fig. 13. Heat transfer enhancement (ζ) is calculated by (Webb, 1981):

$$\zeta = \frac{Nu_p}{Nu_e} \left(\frac{f_e}{f_p} \right)^{1/3} \quad (33)$$

where subscripts p and e denote with and without porous material in heater, respectively. Also, f is the friction factor and calculated by:

$$f = \frac{\Delta p}{0.5 \rho U_m^2 \frac{L}{R_2}} \quad (34)$$

where Δp , U_m and L are the pressure drop, mean velocity and length of the heater, respectively. Note that the Eq. (33) is presented for a constant pumping power. It is observed that the heat transfer enhancement increases with an increase in Darcy numbers. In this figure, ζ greater than 1 indicates that the insert of porous layer inside the channel is suitable in terms heat transfer enhancement and pressure drop.

As a result, the wall temperature decreases by adding the porous material because the heat transfer rate increases with insert of porous layer inside the channel. This also assists to decrease the loss from the heater and leads to increase in the overall solar heater efficiency. Beside this, the porous materials are widely used for purification of liquids and gases. In the heater, these materials have many impacts on the device efficiency and can be utilized as purification of fluids within such devices that leads to mitigation or prevention of corrosion and scaling. The corrosion has the negative impacts on the performance of heaters (Rashidi et al., 2015a).

6. Conclusion

Combined convection–radiation heat transfer in a porous solar heater has been studied in details. Full filled (with

porous substrates), partially filled and empty heaters are considered. This research was performed based on the viewpoints of the heat transfer enhancement and pressure drop for an inserted porous substrate inside the solar heater. The important findings of this research are listed as follows:

- The streamlines within the porous substrate are more elongated in the horizontal direction for high Darcy numbers (i.e. $Da = 10^{-2}$).
- The velocity increases in the fluid region with increase in porous substrate thickness for $\delta = 1/3$ and $2/3$.
- The size of the thermally entrance zone increases with an increase in Darcy number.
- For a constant porous substrate thickness, the divergence between the velocity profiles around the interface region increases with a decrease in Darcy number.
- Nusselt number increases with an increase in the porous substrate thicknesses for higher Darcy number. These augmentations are up to 3, 4.4 and 5.9 times for $\delta = 1/3$, $2/3$ and 1, respectively at $Da = 10^{-2}$.
- Nusselt number decreases with an increase in the porous substrate thicknesses for lower Darcy number (i.e. $Da = 10^{-5}$).
- The averaged Nusselt number increases with an increase in radiation parameter. These augmentations are in the vicinity of 78.8%, 61.8% and 44.4% for Darcy numbers equal to 10^{-4} , 10^{-3} and 10^{-2} , respectively at $0.5 < \lambda < 0.9$.
- The pressure drop for heater increases with an increase in dimensionless porous layer thickness and decrease in Darcy number.

The authors hope that the results from this research provides the useful guidelines to design of solar heat exchangers and can be used as initial data for optimization analysis to calculate the optimum conditions for maximum heat transfer rate and minimum pressure drop.

Acknowledgments

This research was supported by the Office of the Vice Chancellor for Research, Ferdowsi University of Mashhad, under Grant No. 37230. The authors are grateful to Ms. Emily Christian for assistance in editing the manuscript.

Appendix A

The radiative heat transfer could be treated as a diffusion process by introducing the radiative conductivity in cellular porous materials and metallic foams (Nield and Kuznetsov, 2010; Dehghan et al., 2015). A radiative heat flux has been considered at the top wall of the heater in this paper. The boundary condition at this wall is:

$$-(k_c + k_r) \frac{\partial T_2}{\partial y} = q_w''$$

k_r is radiative conductivity and defined by (Nield and Kuznetsov, 2010; Dehghan et al., 2015):

$$k_r = \frac{16\sigma T_w^{*3}}{3\beta_R}$$

k_c is molecular thermal conductivity. The radiative effects inside the porous medium are modeled at energy equation. The energy equation in porous medium can be written as:

$$\frac{1}{\varepsilon} \left(\varepsilon \frac{\partial T_2}{\partial t} + u_2 \frac{\partial T_2}{\partial x} + v_2 \frac{\partial T_2}{\partial y} \right) = \frac{Rc}{RePr} \left(\frac{\partial^2 T_2}{\partial x^2} + \frac{\partial^2 T_2}{\partial y^2} \right)$$

Rc in energy equation is thermal conductivity ratio and is calculated by (Nield and Kuznetsov, 2010; Dehghan et al., 2015):

$$Rc = \frac{(k_c + k_r)}{k_f} f(T)$$

T is dimensionless temperature and calculated by:

$$T = \frac{T^* - T_w^*}{T_m^* - T_w^*}$$

T_m is bulk mean temperature defined by Eq. (12). $f(T)$ is defined by (Nield and Kuznetsov, 2010):

$$f(T) = 1 + b_1 T + b_2 T^2 + b_3 T^3$$

$$b_1 = 3\lambda T_r, \quad b_2 = 3\lambda T_r^2, \quad b_3 = \lambda T_r^3,$$

λ is radiation parameter defined by Eq. (21) and T_r is temperature variation parameter calculated by (Nield and Kuznetsov, 2010):

$$T_r = \frac{T_m^* - T_w^*}{T_w^*}.$$

References

- Acir, A., Ata, I., 2015. A study of heat transfer enhancement in a new solar air heater having circular type turbulators. *J. Energy Inst.*, 1–11.
- Aghajani Delavar, M., Mohammadvali, F., 2013. Numerical simulation of force convection in a channel with porous part. *Int. J. Therm. Environ. Eng.* 6 (1), 7–14.
- Aguiar-Madera, C.G., Valdés-Parada, F.J., Goyeau, B., Ochoa-Tapia, J. A., 2011. Convective heat transfer in a channel partially filled with a porous medium. *Int. J. Therm. Sci.* 50, 1355–1368.
- Alazmi, B., Vafai, K., 2001. Analysis of fluid flow and heat transfer interfacial conditions between a porous medium and a fluid layer. *Int. J. Heat Mass Transfer* 44 (9), 1735–1749.
- Alkam, M.K., Al-Nimr, M.A., 1998a. Transient non-Darcian forced convection flow in a pipe partially filled with a porous material. *Int. J. Heat Mass Transfer* 41 (2), 347–356.
- Alkam, M.K., Al-Nimr, M.A., 1999. Solar collectors with tubes partially filled with porous substrates. *J. Solar Energy Eng.* 121, 20–24.
- Al-Nimr, M.A., Alkam, M.K., 1998b. Unsteady non-darcian fluid flow in parallel-plates channels partially filled with porous materials. *Heat Mass Transfer* 33, 315–318.
- Al-Sumaily, G.F., Sheridan, J., Thompson, M.C., 2012. Analysis of forced convection heat transfer from a circular cylinder embedded in a porous medium. *Int. J. Therm. Sci.* 51, 121–131.
- Bahreghmand, D., Ameri, M., Gholampour, M., 2015. Energy and exergy analysis of different solar air collector systems with forced convection. *Renew. Energy* 83, 1119–1130.
- Banerjee, A., Bala Chandran, R., Davidson, J.H., 2015. Experimental investigation of a reticulated porous alumina heat exchanger for high temperature gas heat recovery. *Appl. Therm. Eng.* 75, 889–895.
- Bejan, A., 2013. *Convection Heat Transfer*, fourth ed. Wiley.
- Bhutta, M.M.A., Hayat, N., Bashir, M.H., Khan, A.R., Ahmad, K.N., Khan, S., 2012. CFD applications in various heat exchangers design: a review. *Appl. Therm. Eng.* 32, 1–12.
- Bovand, M., Rashidi, S., Esfahani, J.A., 2015a. Enhancement of heat transfer by nanofluids and orientations of the equilateral triangular obstacle. *Energy Convers. Management* 97, 212–223.
- Bovand, M., Rashidi, S., Dehghan, M., Esfahani, J.A., Valipour, M.S., 2015b. Control of wake and vortex shedding behind a porous circular obstacle by exerting an external magnetic field. *J. Magnetism Magnetic Mater.* 385, 198–206.
- Brilakis, I., Fathi, H., Rashidi, A., 2011. Progressive 3D reconstruction of infrastructure with videogrammetry. *J. Autom. Constr.* 20, 884–895.
- Chen, X., Sutton, W.H., 2005. Enhancement of heat transfer: combined convection and radiation in the entrance region of circular ducts with porous inserts. *Int. J. Heat Mass Transfer* 48, 5460–5474.
- Chumpia, A., Hooman, K., 2015. Performance evaluation of tubular aluminum foam heat exchangers in single row arrays. *Appl. Therm. Eng.* 85, 121–130.
- Dehghan, M., Tajik Jamal-Abad, M., Rashidi, S., 2014. Analytical interpretation of the local thermal non-equilibrium condition of porous media imbedded in tube heat exchangers. *Energy Convers. Management* 85, 264–271.
- Dehghan, M., Rahmani, Y., Ganji, D.D., Saedodin, S., Valipour, M.S., Rashidi, S., 2015. Convection–radiation heat transfer in solar heat exchangers filled with a porous medium: homotopy perturbation method versus numerical analysis. *Renew. Energy* 74, 448–455.
- Dukhan, N., Bagci, O., Ozdemir, M., 2015. Thermal development in open-cell metal foam: an experiment with constant wall heat flux. *Int. J. Heat Mass Transfer* 85, 852–859.
- Fuqiang, W., Jianyu, T., Lanxin, M., Yong, S., Heping, T., Yu, L., 2014. Thermal performance analysis of porous medium solar receiver with quartz window to minimize heat flux gradient. *Solar Energy* 108, 348–359.
- Hirasawa, S., Tsubota, R., Kawanami, T., Shirai, K., 2013. Reduction of heat loss from solar thermal collector by diminishing natural convection with high-porosity porous medium. *Solar Energy* 108, 305–313.
- Jen, T.C., Yan, T.Z., 2005. Developing fluid flow and heat transfer in a channel partially filled with porous medium. *Int. J. Heat Mass Transfer* 48, 3995–4009.
- Kumar, A., Kim, M.H., 2015. Convective heat transfer enhancement in solar air channels. *Appl. Therm. Eng.* 89, 239–261.
- Lee, T., Lim, S., Shin, S., Sadowski, D.L., Abdel-Khalik, S.I., Jeter, S.M., Al-Ansary, H., 2015. Numerical simulation of particulate flow in interconnected porous media for central particle-heating receiver applications. *Solar Energy* 113, 14–24.
- Li, K., Li, T., Tao, H., Pan, Y., Zhang, J., 2015. Numerical investigation of flow and heat transfer performance of solar water heater with elliptical collector tube. *Energy Proc.* 70, 285–292.
- Mahdavi, M., Saffar-Avval, M., Tiari, S., Mansoori, Z., 2014. Entropy generation and heat transfer numerical analysis in pipes partially filled with porous medium. *Int. J. Heat Mass Transfer* 79, 496–506.
- Martinopoulos, G., Missirlis, D., Tsilingiridis, G., Yakinthos, K., Kyriakis, N., 2010. CFD modeling of a polymer solar collector. *Renew. Energy* 35, 1499–1508.
- Missirlis, D., Donnerhack, S., Seite, O., Albanakis, C., Sideridis, A., Yakinthos, K., Goulas, A., 2010. Numerical development of a heat transfer and pressure drop porosity model for a heat exchanger for aero engine applications. *Appl. Therm. Eng.* 30, 1341–1350.
- Missirlis, D., Martinopoulos, G., Tsilingiridis, G., Yakinthos, K., Kyriakis, N., 2014. Investigation of the heat transfer behaviour of a polymer solar collector for different manifold configurations. *Renew. Energy* 68, 715–723.

- Nield, D.A., Kuznetsov, A.V., 2010. Forced convection in cellular porous materials: effect of temperature-dependent conductivity arising from radiative transfer. *Int. J. Heat Mass Transfer* 53, 2680–2684.
- Patankar, S.V., 1980. *Numerical Heat Transfer and Fluid Flow*. Hemisphere, New York.
- Rashidi, S., Esfahani, J.A., 2015. The effect of magnetic field on instabilities of heat transfer from an obstacle in a channel. *J. Magnetism Magnetic Mater.* 391, 5–11.
- Rashidi, A., Fathi, H., Brilakis, I., 2011. Innovative stereo vision-based approach to generate dense depth map of transportation infrastructure. *Transp. Res. Rec. J. Transp. Res. Board* 2215, 93–99.
- Rashidi, S., Tamayol, A., Valipour, M.S., Shokri, N., 2013. Fluid flow and forced convection heat transfer around a solid cylinder wrapped with a porous ring. *Int. J. Heat Mass Transfer* 63, 91–100.
- Rashidi, S., Bovand, M., Pop, I., Valipour, M.S., 2014a. Numerical simulation of forced convective heat transfer past a square diamond-shaped porous cylinder. *Transport Porous Media* 102 (2), 207–225.
- Rashidi, S., Masoodi, R., Bovand, M., Valipour, M.S., 2014b. Numerical study of flow around and through a porous diamond cylinder with different apex angles. *Int. J. Numer. Methods Heat Fluid Flow* 24 (7), 1504–1518.
- Rashidi, A., Rashidi-Nejad, H., Maghiar, M., 2014c. Productivity estimation of bulldozers using generalized linear mixed models. *KSCE J. Civ. Eng* 18 (6), 1580–1589.
- Rashidi, S., Bovand, M., Esfahani, J.A., 2015a. Heat transfer enhancement and pressure drop penalty in porous solar heat exchangers: a sensitivity analysis. *Energy Convers. Management* 103, 726–738.
- Rashidi, S., Nouri-Borujerdi, A., Valipour, M.S., Ellahi, R., Pop, I., 2015b. Stress-jump and continuity interface conditions for a cylinder embedded in a porous medium. *Transport Porous Media* 107 (1), 171–186.
- Rashidi, S., Dehghan, M., Ellahi, R., Riaz, M., Jamal-Abad, M.T., 2015c. Study of stream wise transverse magnetic fluid flow with heat transfer around an obstacle embedded in a porous medium. *J. Magnetism Magnetic Mater.* 378, 128–137.
- Rashidi, S., Bovand, M., Esfahani, J.A., Öztop, H.F., Masoodi, R., 2015d. Control of wake structure behind a square cylinder by magnetohydrodynamics. *ASME J. Fluids Eng.* 137 (6), 061102–061108.
- Rashidi, S., Bovand, M., Esfahani, J.A., 2015e. Structural optimization of nanofluid flow around an equilateral triangular obstacle. *Energy*. <http://dx.doi.org/10.1016/j.enconman.2015.07.019>.
- Torabi, M., Zhang, K., Yang, G., Wang, J., Wu, P., 2015. Heat transfer and entropy generation analyses in a channel partially filled with porous media using local thermal non-equilibrium model. *Energy* 82, 922–938.
- Tsinoglou, D.N., Koltsakis, G.C., Missirlis, D.K., Yakinthos, K.J., 2004a. Modelling of flow distribution during catalytic converter light-off. *Int. J. Vehicle Design* 34, 231–259.
- Tsinoglou, D.N., Koltsakis, G.C., Missirlis, D.K., Yakinthos, K.J., 2004b. Transient modelling of flow distribution in automotive catalytic converters. *Appl. Math. Modell.* 28, 775–794.
- Valipour, M.S., Rashidi, S., Masoodi, R., 2014a. Magnetohydrodynamics flow and heat transfer around a solid cylinder wrapped with a porous ring. *ASME J. Heat Transfer* 136, 062601–062609. <http://dx.doi.org/10.1115/1.4026371>.
- Valipour, M.S., Rashidi, S., Bovand, M., Masoodi, R., 2014b. Numerical modeling of flow around and through a porous cylinder with diamond cross section. *Eur. J. Mech. B/Fluids* 46, 74–81.
- Wang, F., Shuai, Y., Tan, H., Zhang, X., Mao, Q., 2013. Heat transfer analyses of porous media receiver with multi-dish collector by coupling MCRT and FVM method. *Solar Energy* 93, 158–168.
- Webb, R.L., 1981. Performance evaluation criteria for use of enhanced heat transfer surfaces in heat exchanger design. *Int. J. Heat Mass Transfer* 24, 715–726.
- Xu, H.J., Qu, Z.G., Tao, W.Q., 2014. Numerical investigation on self-coupling heat transfer in a counter-flow double-pipe heat exchanger filled with metallic foams. *Appl. Therm. Eng.* 66 (1–2), 43–54.